Atmospheric Drivers of Tasman Sea Marine Heatwaves

CATHERINE H. GREGORY,[a,b] NEIL J. HOLBROOK,[a,b] ANDREW G. MARSHALL,[b,c] AND CLAIRE M. SPILLMAN[b,d]

[a] *Institute for Marine and Antarctic Studies, University of Tasmania, Hobart, Tasmania, Australia*
[b] *Australian Research Council Centre of Excellence for Climate Extremes, University of Tasmania, Hobart, Tasmania, Australia*
[c] *Bureau of Meteorology, Hobart, Tasmania, Australia*
[d] *Bureau of Meteorology, Melbourne, Victoria, Australia*

(Manuscript received 14 July 2022, in final form 1 March 2023, accepted 29 March 2023)

ABSTRACT: Marine heatwaves (MHWs) can severely impact marine biodiversity, fisheries, and aquaculture. Consequently, there is an increasing desire to understand the drivers of these events to inform their predictability so that proactive decisions may be made to reduce potential impacts. In the Tasman Sea (TS), several relatively intense and broad-scale MHWs have caused significant damage to marine fisheries and aquaculture industries. To assess the potential predictability of these events, we first determined the main driver of each MHW event in the TS from 1993 to 2021. We found that those MHWs driven by ocean advection—approximately 45% of all events—are generally longer in duration and less intense and affected a smaller area compared with the remaining 55%, which are driven by air–sea heat fluxes, are shorter in duration, and are more surface intense. As ocean advection–driven events in the TS have been closely studied and reported previously, we focus here on atmospherically driven MHWs. The predictability of these events is assessed by identifying the patterns of atmospheric pressure, winds, and air–sea heat fluxes in the Southern Hemisphere that coincide with MHWs in the Tasman Sea. We found that atmospherically driven MHWs in this region are more likely to occur during the positive phase of the asymmetric Southern Annular Mode (A-SAM)—which presents as an atmospheric zonal wave-3 pattern and is more likely to occur during La Niña years. These A-SAM events are linked to low wind speeds and increased downward solar radiation in the TS, which lead to increased surface ocean temperatures through the reduction of mixing.

SIGNIFICANCE STATEMENT: The purpose of this study is to understand factors of the atmosphere that contribute to an accumulation of heat in the upper ocean in the Tasman Sea to better inform predictability. Higher incidences of ocean extreme thermal events (known as marine heatwaves) in this region are becoming increasingly more common and threatening the important marine industries that support the people of both Australia and New Zealand. We need to know the sources of this extra heat to understand whether such events can be predicted. Previous studies have found the East Australian Current to be responsible for around half of these events, and our results show a connection between a known atmospheric pattern and the other half. As we continue to improve our ability to anticipate this pattern, this suggests that we may also be able to predict these extreme heating events.

KEYWORDS: Antarctic Oscillation; Atmosphere–ocean interaction; Heatwave; Seasonal forecasting; Climate variability; Subseasonal variability

1. Introduction

The Tasman Sea is a global warming hotspot (Hobday and Pecl 2014). This renders the region susceptible to increased incidences of marine heatwaves (MHWs), such as the extreme events that occurred in the summers of 2015/16 (Oliver et al. 2017), 2017/18 (Perkins-Kirkpatrick et al. 2019; Kajtar et al. 2022), and 2018/19 (Salinger et al. 2020). The impacts of these extreme events include the local extinction of bull kelp in New Zealand (Thomsen et al. 2019) and an outbreak of Pacific oyster mortality syndrome in Tasmania, leading to loss of jobs (Smith et al. 2021) and mortality of blacklip abalone and poor performance of salmon (Oliver et al. 2017). Tasmania, the southern island state of Australia, is home to salmon aquaculture businesses that represent Australia's most valuable seafood industry (Australian Bureau of Agricultural and Resource Economics and Sciences 2014). The industry has been increasingly threatened with rising oceanic temperatures and, more recently, strong public scrutiny (Cullen-Knox et al. 2019). To proactively address pressures from short-term variability, seasonal forecasting models have been developed to aid management decision-making (Spillman and Hobday 2014). With industries increasingly reliant on forecast tools, it is important that they are as accurate as possible to provide stakeholders with reliable information so that harm minimization strategies might be considered and implemented. The potential reliable time scale of these MHW forecasting tools is determined by the main drivers of the events, with regions dominated by oceanic processes expected to have a longer time scale of predictability than those more strongly influenced by the atmosphere (Holbrook et al. 2020).

An MHW is a discrete and prolonged warm ocean extreme event. MHWs have been increasing globally in frequency, duration, and intensity (Oliver et al. 2018a), largely due to

Supplemental information related to this paper is available at the Journals Online website: https://doi.org/10.1175/JCLI-D-22-0538.s1.

Corresponding author: Catherine H. Gregory, catherine.gregory@utas.edu.au

DOI: 10.1175/JCLI-D-22-0538.1

background global ocean warming (Oliver 2019). The parameters used to describe individual events depend on the purpose of the study, with research seeking to understand long-term climatic trends generally incorporating a monthly definition (Scannell et al. 2016; Jacox et al. 2020; Xu et al. 2021), and those focused on understanding direct impacts and short-term variability using a daily definition (Arias-Ortiz et al. 2018; Smale et al. 2019; Schlegel et al. 2021). The most common method used to detect MHWs was established by Hobday et al. (2016a), where an MHW in a region is defined when the sea surface temperature (SST) exceeds a 90th percentile threshold, relative to a seasonally varying climatology of at least 30 years, for five or more days.

The dynamical nature of the ocean complicates the making of reliable forecasts. The main contributors to anomalously high ocean temperatures are the intensified advection of poleward currents, transporting warmer water to higher latitudes, and enhanced net downward air–sea fluxes due to increased atmospheric temperatures, increased exposure to solar radiation due to decreased cloud cover, and reduced latent heat loss due to decreased winds (Holbrook et al. 2019). In the Tasman Sea, it has been found that approximately half of all MHWs are due to ocean advection, associated with an intensified extension of the East Australian Current (EAC) (Oliver et al. 2017; Li et al. 2020), while the remaining half are primarily surface heat flux driven. While those events driven by increased advection tend to be more localized in the western Tasman Sea off the east coast of Tasmania (such as the 2015/16 MHW), those driven by air–sea heat fluxes may impact an extended area reaching from Tasmania to New Zealand (Perkins-Kirkpatrick et al. 2019). By understanding the drivers and lead time scales of atmospherically driven MHWs, we will better understand their potential predictability and increase the likelihood that we will be able to more accurately predict them (Holbrook et al. 2020).

Surface-layer MHWs driven by atmospheric forcing are expected to have shorter lead times than those from oceanic processes (Holbrook et al. 2020). While predictive studies have often either focused on weather prediction time scales (typically limited at 7–10 days) (e.g., Perez et al. 2013) or examined the role of seasonal to interannual climate modes as predictors [e.g., El Niño–Southern Oscillation (ENSO), Indian Ocean dipole, etc.] (e.g., Zhang et al. 2016; Goddard et al. 2001), the intermediate subseasonal to seasonal [S2S; from 10 days to 9 months, including the Madden–Julian oscillation and Southern Annular Mode (SAM)] time scale has often been ignored, but represents an important opportunity going forward, with numerous potential benefits (White et al. 2017). As climate change is becoming an increasingly dominant driver of ocean conditions, long-term, historical changes become less relevant to predict near-future climatic variability where the atmosphere operates on these shorter time scales.

The leading driver of climatic variability in the Southern Hemisphere (SH) is the SAM (Limpasuvan and Hartmann 1999), including strong influences on the Australian climate (Trenberth 1979; Rogers and van Loon 1982; Raut et al. 2014; Mariani and Fletcher 2016). The phases of SAM are determined by the latitudinal location of the strong westerly winds that typically blow in the mid- to high-latitude region of the SH. During the positive SAM phase, these winds contract poleward toward Antarctica, and during the negative phase, they expand toward the equator (Gong and Wang 1999). Changes to these wind patterns can impact rainfall and temperatures over Australia (Hendon et al. 2007; Risbey et al. 2009; Marshall et al. 2012) and have been shown to contribute to the poleward extension of the EAC (Li et al. 2022a). With a positive trend in the tendency for positive SAM phases due to an increase in greenhouse gas forcing and a depleted ozone (Cubasch et al. 2001; Marshall et al. 2004; Son et al. 2009; Karpechko et al. 2010), our need to understand the possible impacts of positive SAM events is intensified. Further, the geographic impacts of SAM strongly vary based on the season (Kidston et al. 2009), the solar cycle (Haigh and Roscoe 2006), and SAM's connection with other modes such as ENSO (L'Heureux and Thompson 2006; Fogt et al. 2011) and the Madden–Julian oscillation (MJO) (Matthews and Meredith 2004).

The aim of this paper is to understand the atmospheric drivers affecting SSTs in the Tasman Sea and their potential to sustain elevated temperatures in the upper ocean, leading to MHWs. The focus on atmospheric processes, at time scales from a week up to several months, enables us to examine MHWs forced on the S2S time scale. By understanding the atmospheric factors contributing to these MHW events, we aim to find their connection to known modes of climatic variability that operate and/or interact on those time scales, thus improving knowledge of their potential predictability and, ultimately, our ability to predict them.

This paper is organized as follows. Section 2 describes the datasets and methodology used, including the calculation of MHW statistics and the separation of events into predominantly ocean advection driven or atmospherically driven. Section 3 examines the general differences between these two groups of MHWs, including their statistical, local, and spatial properties. Section 4 explores the atmospheric patterns in the SH that correspond to SST anomalies similar to those atmospherically driven MHWs found in section 3. Section 5 explores the statistical significance of this relationship and provides a dynamical explanation, and section 6 is a summary and discussion.

2. Data and methods

a. Data

Table 1 summarizes the datasets and climate variables that were used in this study. They are described here. The SST data used to analyze MHWs in this study were from the National Oceanic and Atmospheric Administration (NOAA) high-resolution Optimum Interpolation Sea Surface Temperature (OISST), version 2.1, dataset (Huang et al. 2021a,b). These 0.25° gridded data are from high-resolution infrared and microwave satellites blended with in situ observational data from ships and buoys and comprise daily SSTs from 1982 to the present day (Reynolds et al. 2007; Banzon et al. 2016; Huang et al. 2021b).

TABLE 1. A summary of the climate variables and corresponding datasets used throughout the study.

Variable	Dataset	Spatial resolution	Temporal resolution	Time period used	Source
Sea surface temperature	NOAA's high-resolution OISST v2.1	0.25° lat × 0.25° lon, from 89.875°S to 89.875°N and from 0.125° to 359.875°E	Daily values from 1 Sep 1981 to present	1993–2021	Huang et al. (2021a)
Mean sea level pressure; surface winds	NCEP–NCAR reanalysis	2.5° lat × 2.5° lon, from 0° to 357.5°E and from 90°N to 90°S	4 times daily, daily, and monthly from 1 Jan 1948 to present	1993–2021	Kalnay et al. (1996)
Mixed layer depth	BRAN2020	0.1° lat × 0.1° lon, from 75°S to 75°N, covering all longitudes, with 5-m vertical resolution to 40-m depth and 10-m vertical resolution to 200-m depth	Daily from 1 Jan 1993 to present	1993–2021	Chamberlain et al. (2021)
Sensible heat flux, latent heat flux, surface net downward shortwave radiation, and surface net downward longwave radiation	JRA-55	55-km horizontal resolution, °from 90°S to 90°N, covering all longitudes, with 60 levels from the surface to 0.1-hPa vertical resolution	6 hourly from 1 Jan 1958 to present	1993–2021	Kobayashi et al. (2015)

The heat budget analysis was performed using data from the Bluelink Reanalysis (BRAN) 2020 (Chamberlain et al. 2021). BRAN2020 is an improvement over earlier versions of BRAN (Chamberlain et al. 2021). It is the result of assimilated observations into an eddy-resolving, near-global ocean circulation model [Ocean Forecasting Australia Model v3 (Oke et al. 2013)] to provide daily reanalysis data at 0.1° resolution comprising physical variables such as temperature, velocity, and mixed layer depth (MLD), where the MLD is the depth over which the buoyancy surpasses 0.0003 m s^{-2} (Chamberlain et al. 2021). The Ocean Forecasting Australia Model version 3 (OFAM3) is forced by the atmospheric output from the Japanese Meteorological Agency's Japanese 55-year Reanalysis (JRA-55) (Kobayashi et al. 2015).

The atmospheric data used to calculate the relevant indices, and to investigate the large-scale climate patterns, were taken from the National Centers for Environmental Prediction–National Center for Atmospheric Research (NCEP–NCAR) reanalysis 2 product. This dataset was generated using a forecast model assimilated with observational data (Kanamitsu et al. 2002) and, with a relatively coarse spatial grid of 2.5°, is well suited for analysis of large-scale processes (Dufek et al. 2008). Variables extracted and utilized from the NCEP–NCAR reanalysis include the mean sea level pressure (MSLP) to calculate the SAM index, and the MSLP and surface winds used in a self-organizing map (SOM) analysis discussed later.

b. Calculation of climate indices

1) SAM INDEX

The daily SAM index was calculated by projecting daily MSLP anomalies onto the principal component (PC) time series of the leading empirical orthogonal function (EOF) of observed monthly mean MSLP anomalies between 25° and 75°S (see Marshall et al. 2014). SAM-positive events are identified when the index is one standard deviation or greater above the mean, and SAM-negative events when the index is at least one standard deviation below the mean. Anything in between is characterized as SAM neutral. While there is more variability in the index using daily data, the general structure of the mode does not differ greatly from one generated using monthly values.

2) ENSO INDEX

The phase of ENSO was determined using NOAA's Oceanic Niño Index (ONI) (Bamston et al. 1997). Using a three-month running mean of SST anomalies in the Niño-3.4 region (5°S–5°N, 170°–120°W), an El Niño state is five consecutive months with SST anomalies $>+0.5$°C, with a La Niña state declared with SST anomalies <-0.5°C for the same period length, and all other periods considered neutral (Bamston et al. 1997). The daily ENSO index was calculated as the SST anomalies (temperature deviations from the mean, calculated using the full climatology from 1982 to 2021) in the Niño-3.4 region (5°S–5°N, 170°–120°W) (Philander 1983). El Niño periods were taken as days when the index was more than one standard deviation above the mean and La Niña days when the index fell below negative one standard deviation from the mean.

c. Selection of study region and EOF analysis

Estimates of MHW variability and features vary between studies depending on box average sizes chosen and areas of interest. Here, we aim to assess MHWs separately based on

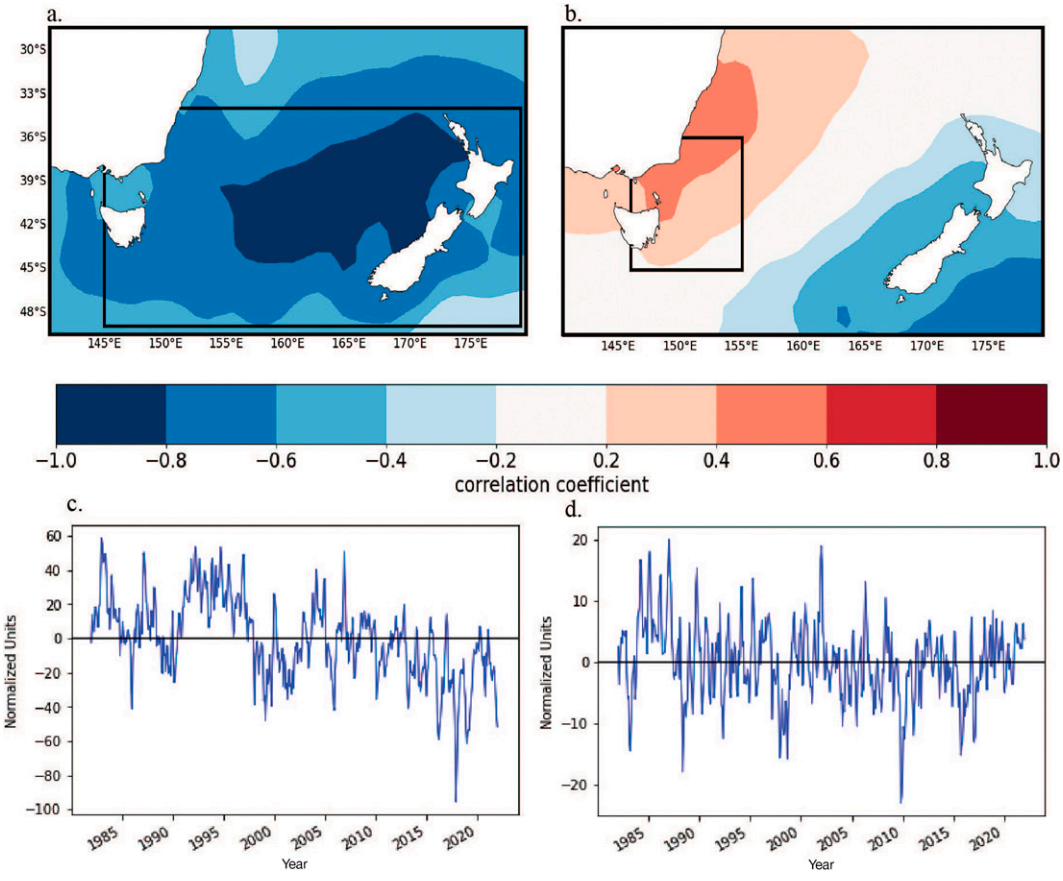

FIG. 1. The first two leading modes from the EOF analysis, expressed as the correlation between each PC and the SST anomalies in the Tasman Sea. (a) The first mode accounts for 36% of the total variance and shows a relatively uniform region, where we define a general Tasman Sea (TS) region (outlined) bound by 35°–50°S and 145°E–180°. (b) The second mode accounts for 14% of the total variance and shows a dipole pattern in which the waters off the southeast coast of Australia are distinctive from those surrounding New Zealand. (c),(d) The corresponding PC. Here we select a region (outlined) labeled as Tasmanian Eastern (TE) bound by 36°–45°S and 146°–155°E, which is likely to be influenced by the EAC Extension as well as by air–sea fluxes.

whether they are primarily driven by ocean advection or air–sea fluxes, and so we chose a broader region (see Fig. 1) impacted by both. EOF analysis allows high-dimensional data to be presented as reoccurring patterns based on the interrelationships within the data (Weare et al. 1976). We performed an EOF analysis on monthly SST anomalies (temperature deviations from the mean, calculated using the full climatology) between 1982 and 2021 to identify patterns in the region to aid selection of our regions of interest.

Figure 1 shows the EOFs expressed as a correlation between the corresponding PCs and SST anomalies at each point in space. The leading EOF of SST anomalies in the Tasman Sea showed a broad monopole encompassing the whole region (Fig. 1a), while the second EOF shows a dipole pattern split between the waters off southeast Australia and the region around New Zealand (Fig. 1b). This allowed for the splitting into two regions, which we refer to as the Tasman Sea (TS) (35°–50°S, 145°E–180°) and Tasmanian Eastern (TE) (36°–45°S, 146°–155°E) boxes. As part of this study aims to compare events driven by enhanced downward air–sea fluxes with those driven primarily by enhanced warm-water advection in the EAC Extension, the heat budget analysis that follows is based on the TE box, as this region is that which is more likely to be impacted by both. However, much of the analysis was still plotted using the larger region to extend the area of MHW predictability to include New Zealand.

d. *Calculation of MHW statistics*

The MHW statistics were computed according to the Hobday et al. (2016a) definition, where a daily climatology and a 90th-percentile threshold is first calculated and any continuous period of five days or greater above the threshold is considered an MHW, with events separated by two days or less still considered as continuous. We performed this analysis on SST values at each grid point in the TS region to include all events and to understand the general spatial patterns of all events. Following this, we performed the same analysis on the area-averaged SST

within the TE region to determine a discrete list of events to be further examined.

The MHW metrics calculated for each event included the duration and the maximum, mean, and cumulative intensities. The start day is taken as the first day that the SST breaches the 90th percentile before being held for at least 5 days. The end day is the final day the SST is sustained for at least 5 days above the 90th percentile. The peak day is taken as the day the event reached its maximum intensity. Each event, therefore, comprises an onset phase (between the start and peak days) and a decline phase (between the peak and end days). From these, the onset and decline rates were recorded in degrees Celsius per day (see Fig. 1 from Hobday et al. (2016a).

The MHW intensity on each day of each event was categorized depending on the extent to which the maximum intensity surpassed the 90th percentile, according to the categorization scheme developed by Hobday et al. (2018a). Category one (moderate) corresponds to an intensity that is less than twice the difference between the climatology and the 90th percentile. Accordingly, category two (strong) corresponds to an intensity between 2 and 3 times this difference, category three (severe) is between three and four times, and category four (extreme) denotes anything above 4 times the difference from the threshold to the climatological mean. This categorization is a useful tool to compare the severity of events across time (Hobday et al. 2018a).

The period selected to base the climatology on can create a bias in the calculated statistics. As the Tasman Sea region off Tasmania is a region of decadal variability and long-term warming (Holbrook and Bindoff 1997; Ridgway 2007), a climatology of the period 1983–2012, for example, used in previous MHW studies (Oliver et al. 2018a; Holbrook et al. 2019; Smale et al. 2019), results in persistent MHWs during summer and spring seasons after 2016. Hence, to provide an unbiased analysis of the background temperature change, we have here used the full period from 1982 to 2021 as the climatological baseline to evaluate MHW events over the same record period, to reflect the changing climate [as per Wang et al. (2022) in their study of trends in marine cold spells].

Figure 2 shows a history of MHWs in the two regions outlined in Fig. 1, together with the Niño-3.4 index. Figure 2a shows the Niño-3.4 index, with the red shaded parts representing El Niño periods and the blue shaded parts, La Niña periods (these periods are also shown as vertical lines in the background of Figs. 2b and 2c). Figures 2b and 2c show all the MHWs from 1982 to 2021 in the greater TS and smaller TE regions, respectively. The maximum MHW category at every grid point was recorded, and bar graphs were produced to show accumulation of these in time. In this way, the height of each of the bars shows the total proportion of area in an MHW state, with the colors showing the highest category reached. All calculations were performed on a daily time scale but converted to monthly for easier depictions.

The increase in strong, severe, and extreme categories toward the later years, and the increased height of the bars, show the increase of maximum intensities and spatial extent of MHWs in the Tasman Sea in recent years. This is most apparent during the two most extreme events on record, during 2015/16 and 2017/18. From Fig. 2c, we see that both these events impacted the entire TE region and reached the extreme categorization, with the 2015/16 event existing in a strong category or above over more than half of the area. Comparing this to the wider TS region in Fig. 2b, we see that while both these events are also relatively significant, the 2017/18 event (as well as the 2019/20 event) impacted a far greater proportion of the entire area.

e. *Correlation between ENSO and SST anomalies in the Tasman Sea*

ENSO is considered the largest contributor to global climate variability (McPhaden et al. 2006). A weak correlation between positive summer ocean temperatures in eastern Tasmania and ENSO has been linked to the strengthening of the EAC (Oliver and Holbrook 2018) and the higher latitude of the EAC's separation from the coast at the relaxation of an El Niño period (Cetina-Heredia et al. 2014). To examine the general state of the Tasman Sea during El Niño and La Niña periods, we composited the SST anomalies of each of the days in the La Niña or El Niño periods, based on the ONI.

Figure 3 shows maps of SST composites, separated by month, from September to February. Maps are masked for statistical significance, with shaded regions showing significance at the 5% level, assessed using a Student's t test (Student 1908). The wider Tasman Sea shows cooler temperatures during El Niño periods, with general positive anomalies during La Niña. There is an almost uniform pattern of warming in La Niña periods during September (Fig. 3b) and January (Fig. 3j). However, most other months show some variability associated with the EAC. This is most apparent in February, where the positive anomalies are more constrained to the western TS region, and October (Fig. 3d), where the positive anomalies are to the south of our domain.

During El Niño periods, there is a wider cooling pattern during September (Fig. 3a) and December (Fig. 3g), and similar patterns to La Niña periods, with this cooling being concentrated farther south in October (Fig. 3c) and to the west in February (Fig. 3k). Positive anomalies are seen near the east coast of Australia and, in November (Fig. 3e) and January (Fig. 3i), near the east coast of Tasmania.

f. *Quantifying the contribution of air–sea flux*

The accumulation of heat in the surface ocean is caused by either ocean advection, i.e., net convergence from currents transporting anomalously warm waters into a particular location, or surface heat flux forcing, where net downward heat flux forcing acts to heat the upper ocean (Holbrook et al. 2019). The relative influence of each of these sources can be considered using the heat budget equation [Eq. (1)], employed in previous MHW studies such as those by Benthuysen et al. (2014) and Oliver et al. (2017):

$$\frac{\partial T}{\partial t} = \frac{Q_{\text{net}}}{\rho C_p H} - \left(u\frac{\partial T}{\partial x} + v\frac{\partial T}{\partial y} + w\frac{\partial T}{\partial z} \right) + \text{res}. \qquad (1)$$

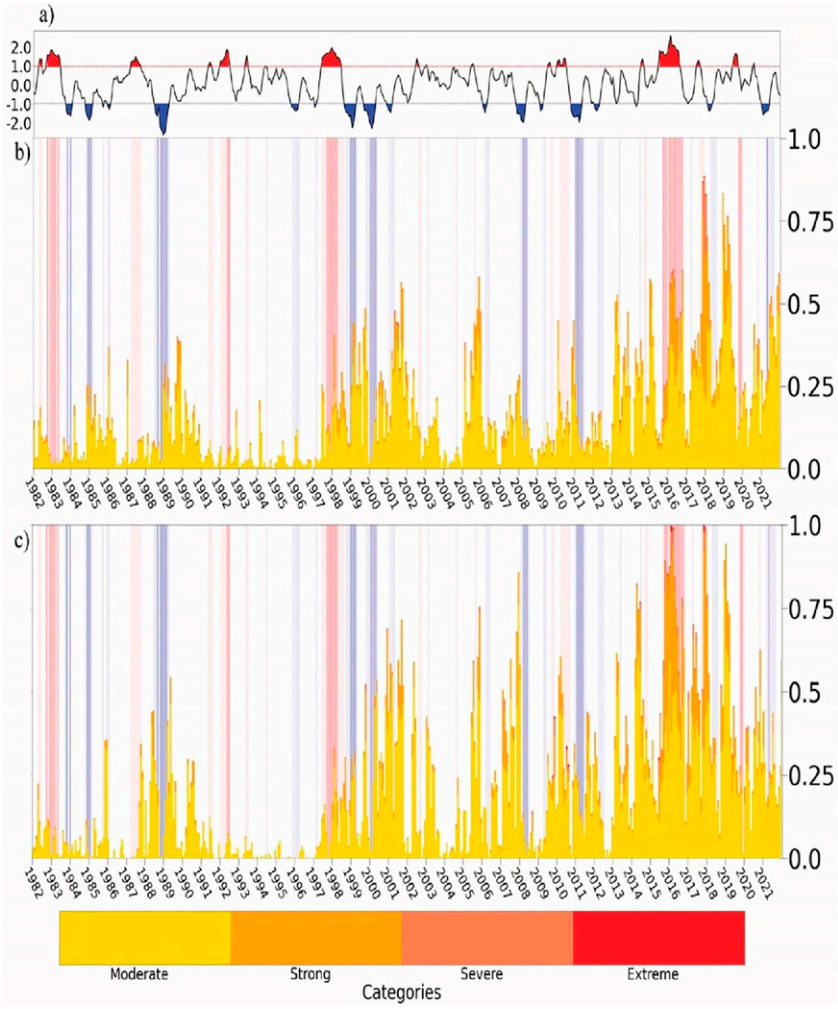

FIG. 2. (a) The Niño-3.4 index showing El Niño periods in red and La Niña periods in blue. The bar graphs show a history of marine heatwaves in (b) the greater TS region and (c) the smaller TE region. The colors represent the maximum category reached. Moderate (yellow) is representative of SST anomaly (SSTA) between 1 and 2 standard deviations above the calculated threshold, strong (orange) is representative of SSTA between 2 and 3 standard deviations above the threshold, severe (coral) is representative of SSTA between 3 and 4 standard deviations above the threshold, and extreme (red) is representative of SSTA greater than 4 standard deviations above the threshold. The height of the bar shows the proportion of area, relative to the total area of the corresponding region, in an MHW state. Also shown are El Niño periods as pink vertical bars and La Niña periods as blue ones in (b) and (c).

Equation (1) shows the time rate of change in temperature due to contributions from the net surface heat flux scaled by the seawater density ρ, heat capacity C_p, and mixed layer depth H (first term on the right-hand side), ocean advection (second term), and other residual factors (res) that contribute to temperature changes such as horizontal and vertical diffusion (third term). The net surface heat flux Q_{net} represents the sum of net contributions from the shortwave (solar) radiation, longwave (thermal) radiation, sensible heat exchange due to the difference between atmospheric and oceanic temperature, and latent heat due to evaporation [Eq. (2)]:

$$Q_{\text{net}} = Q_{\text{SW}} + Q_{\text{LW}} + Q_{\text{Sen}} + Q_{\text{Lat}}. \tag{2}$$

From these equations, we integrated the first term on the right-hand side of the heat budget equation [Eq. (1)] during the MHW onset period (for n days) to understand the relative contribution of the air–sea heat fluxes:

$$T_{Q_{\text{net}}} = \int_{t=0}^{t=n} \frac{Q_{\text{net}}}{\rho C_p H}\, dt. \tag{3}$$

Following this, we integrated the horizontal ocean advection terms during the same period, separated into the zonal (u) and meridional (v) components:

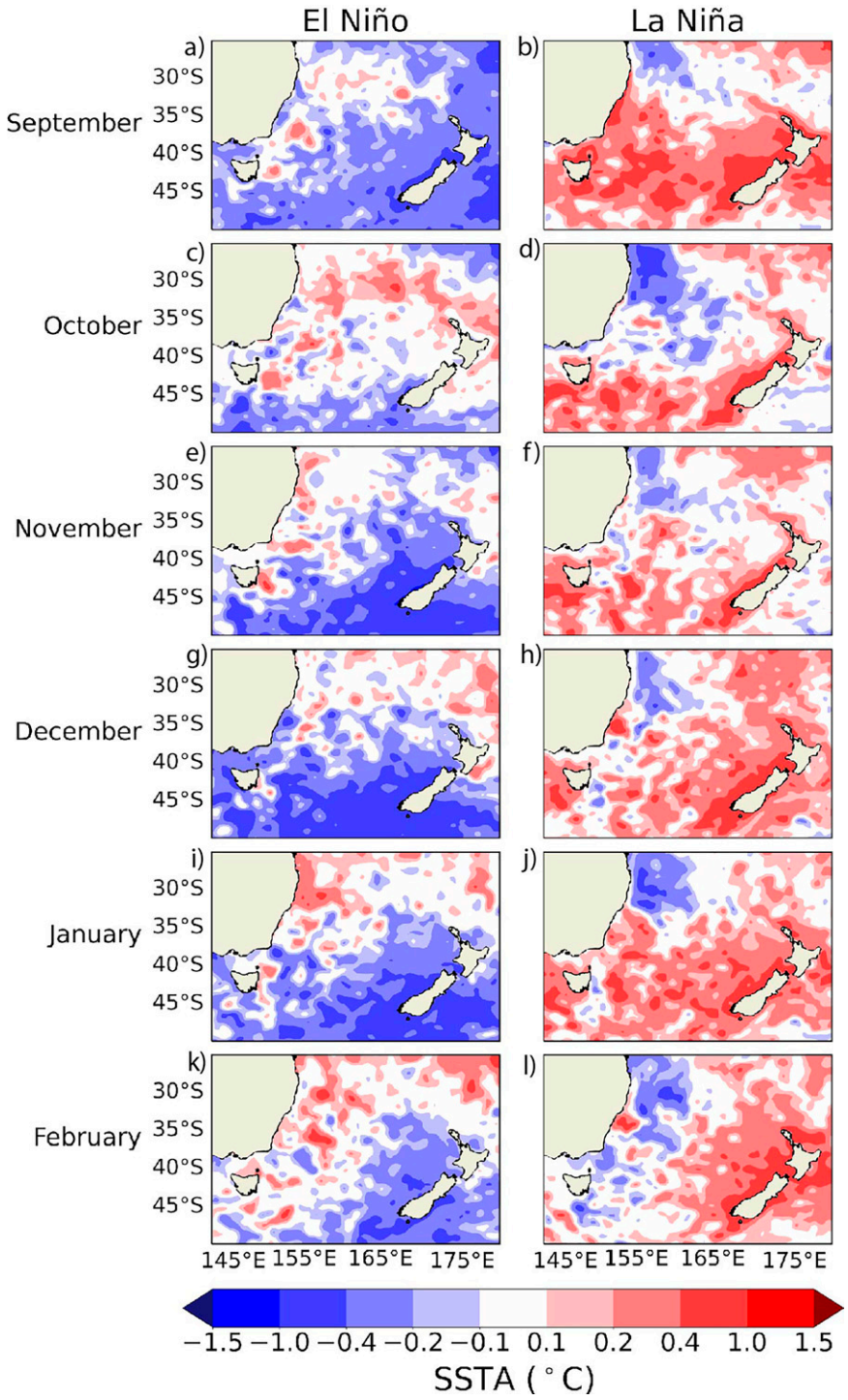

FIG. 3. Composite maps showing the SST anomalies during El Niño and La Niña periods, separated by month, from September to February.

$$T_{\text{adv\_}u} = \int_{t=0}^{t=n} u\frac{\partial T}{\partial x}\,dt \quad \text{and} \tag{4}$$

$$T_{\text{adv\_}v} = \int_{t=0}^{t=n} v\frac{\partial T}{\partial y}\,dt. \tag{5}$$

We used a variable MLD in this analysis as it has been shown that fixing this depth can influence the identification of an MHW driver by amplifying the contribution of the air–sea flux when the MLD is underestimated and dampening its contribution when the MLD is overestimated (Elzahaby et al. 2022).

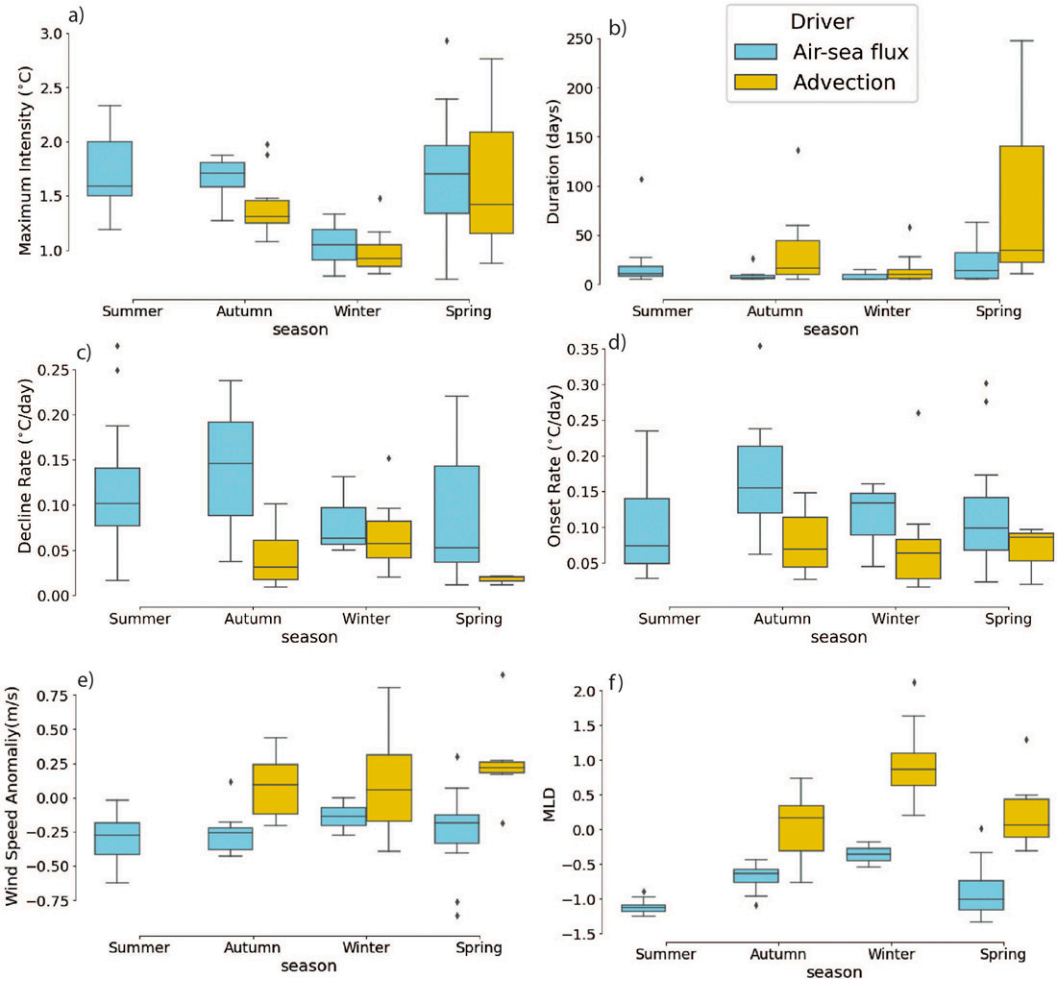

FIG. 4. Box-and-whisker plots showing the average (a) maximum intensity, (b) duration, (c) decline rate, (d) onset rate, (e) wind speed anomaly, and (f) MLD anomaly (standardized) during the buildup phase of all MHWs in the TE region, separated by the season in which they began. MHWs primarily driven by air–sea fluxes (n = 38 events) are blue, and those driven by advection (n = 31 events) are yellow.

By comparing the relative contributions from the air–sea flux and advection components during the onset phase of each of the MHW events, we were able to determine the main driver of each event. For a complete list of these events and their drivers, see Table S1 in the online supplemental material.

g. *Self-organizing maps*

SOMs are an artificial neural network technique commonly used in climate science and oceanography to reduce high-dimensional input data to a lower-dimensional output of commonly occurring and/or synoptic patterns (Kohonen 1990; Oliver et al. 2018b; Udy et al. 2021). They use unsupervised machine learning to sort many datasets into groups by identifying potential clusters and shapes and continually moving each dataset until it is placed in a group, known as a node, with other datasets of greatest similarity (Allinson et al. 2012). They have been shown to have the advantage over principal component analysis as they are better able to isolate synoptic weather patterns and are less likely to mix patterns together (Reusch et al. 2005). For details of the SOMs algorithm, see the methods section of Cassano et al. (2006) and Verdon-Kidd and Kiem (2009).

MHWs in the Tasman Sea and off the east coast of South America have been, respectively, linked to atmospheric patterns across the Southern Ocean, including wavenumber-4 patterns of high and low pressure systems separated by approximately 90° longitude during summer (Chiswell 2021) and atmospheric blocking, and anomalous anticyclonic circulation associated with tropical–extratropical atmospheric Rossby wave trains (Rodrigues et al. 2019), both detectable as patterns of MSLP anomalies. Here, we analyzed SOMs with daily MSLP anomalies to find the atmospheric patterns connected to MHWs in the Tasman Sea.

We used the SOMs algorithm in the R package *Kohonen* (Wehrens and Kruisselbrink 2018), which requires a number

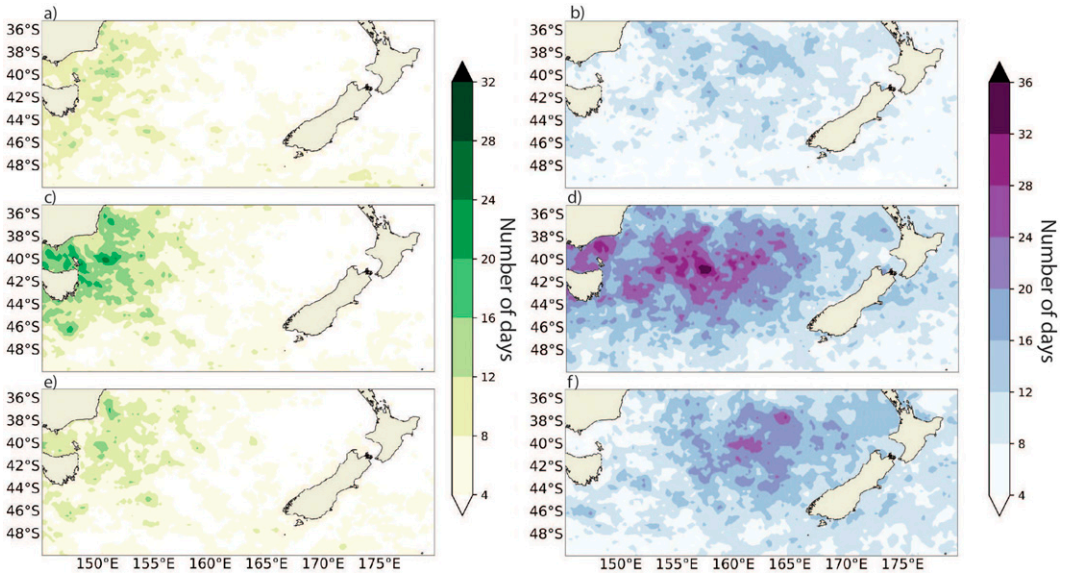

FIG. 5. Density plots showing the number of days that each grid point is above the 90th-percentile threshold during different stages of MHW events, giving the total pixel count for (a),(c),(e) the 31 MHW events driven primarily by ocean advection and (b),(d),(f) the 38 MHW events driven by air–sea fluxes on the (top) start, (middle) peak, and (bottom) end days.

of nodes in a grid structure ($m \times n$) to find the representation of the main observable patterns. The number of nodes selected is an important decision that strongly influences the variety of patterns produced. Too few nodes would result in only general, large-scale climate patterns being recognized, while too many nodes produce repeated patterns. As we wanted to identify atmospheric patterns associated with oceanic extremes—that statistically should occur less than 10% of the time, as we used a 90th-percentile threshold—it was necessary that we selected a high enough number of nodes to separate the data into roughly 10 nodal patterns. Following sensitivity testing, an optimal grid size of 3×3 (9 nodes) was chosen. Pearson pattern correlations were used to quantitatively justify the patterns of each node by comparing the pattern of each day to the composite pattern produced for each node. It was found that the average correlation score for each node was greater than 0.8 (Fig. S1 in the online supplemental material). After the algorithm sorted each daily MSLP anomaly dataset to its node, composite maps were made of the corresponding observed daily surface wind and SST anomalies of each of the nodes.

3. Key drivers of marine heatwaves

a. *Marine heatwave properties*

In total, there were 69 MHW events detected in the TE box from 1993 to 2021. Using the heat budget analysis [Eq. (1)] to determine the main source of excess heat during the onset phase of each MHW, we found that 38 (55%) of the events were primarily driven by air–sea heat fluxes and the remaining 31 (45%) by ocean advection. We separated the events by the season in which they began (i.e., their start date) and found that during austral autumn [March–May (MAM)], winter [June–August (JJA)], and spring [September–November (SON)], there was an even spread of events in each group. However, all events that began during austral summer [December–February (DJF)] were found to be driven by air–sea fluxes. This is not to say that there were no advection-driven MHW occurrences during summer, as many of those events which began in spring continued into the summer months.

We found several noticeable differences between the TE MHWs driven by air–sea heat fluxes when compared with those driven by ocean advection (Fig. 4). Those driven by air–sea fluxes had a higher average SST maximum (Fig. 4a), average intensity, and cumulative intensity (not shown) and shorter durations (Fig. 4b) in all seasons. The longest and most intense events began during spring. Both the onset (Fig. 4d) and decline rates (Fig. 4c) for air–sea flux–driven MHW events were generally faster. As these atmospherically driven events have, on average, high intensities, their typically faster onset rates suggest that the onset phase for these events persists for a shorter duration of time than those driven by ocean advection (see Fig. 1 from Hobday et al. 2016a).

Weaker winds (Fig. 4e) and a shallower MLD (Fig. 4f) correspond with the onset of MHWs driven by air–sea fluxes, with both variables showing negative anomalies for all these events. Decreased winds reduce mixing in the upper layers of the ocean and so decrease the amount of heat transported to depth, hence allowing the MLD to shoal (Carton et al. 2008). This also allows a shallower MLD to precondition the ocean for an MHW, as this relatively lower volume of water within the mixed layer can be heated more readily (Holbrook et al. 2019; Sen Gupta et al. 2020).

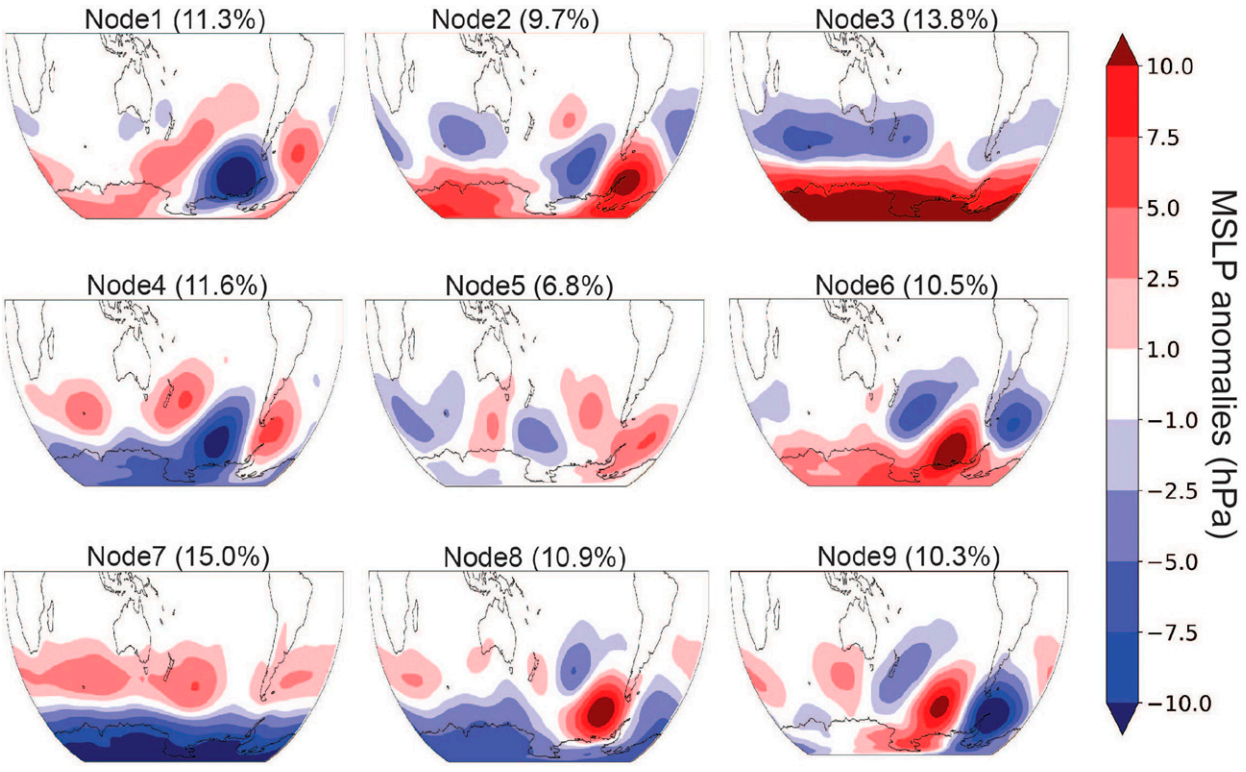

FIG. 6. SOMs of MSLP anomalies (hPa) in the SH during austral spring, with the percentage shown indicating the total frequency of each SOM node. The main nodes of interest are node 3, which shows a negative SAM pattern, and nodes 4 and 7, which show two different forms of positive SAM.

b. Spatial extents

The frequency of each grid point above the 90th-percentile threshold for each MHW event at the start, peak, and end date was counted at each grid point and mapped to show the regions typically most impacted during ocean advection or air–sea flux–driven events. Those events driven by ocean advection are seen to predominantly impact the region off the eastern coast of Tasmania, without extending far enough to influence the waters surrounding New Zealand (Fig. 5, left). Events driven by air–sea fluxes, however, occupy a much larger area, reaching the west coast of New Zealand and even extending farther east (Fig. 5, right).

4. Connecting atmospheric states with MHWs

Based on the SOM analysis, the nine MSLP anomaly nodes were analyzed to identify which of the common atmospheric patterns across the Southern Ocean were associated with elevated SSTs in the Tasman Sea. As previously mentioned, the most severe MHW events (of both highest duration and intensity) began in the austral spring (SON), and so here we focus on understanding the atmospheric patterns during these months. Figure 6 shows the nine most common patterns of MSLP anomalies during austral spring and their frequency. Node 3 is recognized as a negative SAM pattern. However, nodes 4 and 7 show a positive expression of SAM. Both nodes show negative pressure anomalies over Antarctica, with positive pressures at the mid- to high latitudes. While node 7 shows the classic positive SAM pattern, node 4 shows these high pressure anomalies in an atmospheric wave-3 pattern.

Figure 7 shows the corresponding surface wind speed anomalies from the nine nodes of the MSLP anomalies. The wind patterns strongly resemble those described in relation to the phases of SAM in previous literature (Kidston et al. 2009). Node 3 shows a band of negative wind speed anomalies over most of the Southern Ocean, with stronger winds in the mid- to high latitudes, including across the Tasman Sea. While nodes 4 and 7 are synonymous with a positive SAM pattern, their wind patterns are distinctly regional. Node 4 shows negative wind anomalies across the Tasman Sea, while the midlatitude negative wind anomalies from node 7 are farther to the west.

The nine SOM nodes of the SST anomalies (Fig. 8) show the thermal oceanic patterns that correspond with these atmospheric patterns. In most of the nodes, we can see slight (between 0.25° and 0.5°C) positive SST anomalies associated with the EAC Extension. This suggests that there is no dominant atmospheric pattern connected with those MHWs which are ocean advection driven. However, we can clearly see the strong SST anomalies (between 0.5° and 1.5°C) that stretch across most of the Tasman Sea in node 4, with a similar spatial pattern to air–sea heat flux–driven MHW events (Fig. 5). This suggests there may be a connection between a regional variation of positive SAM and MHWs in the Tasman Sea.

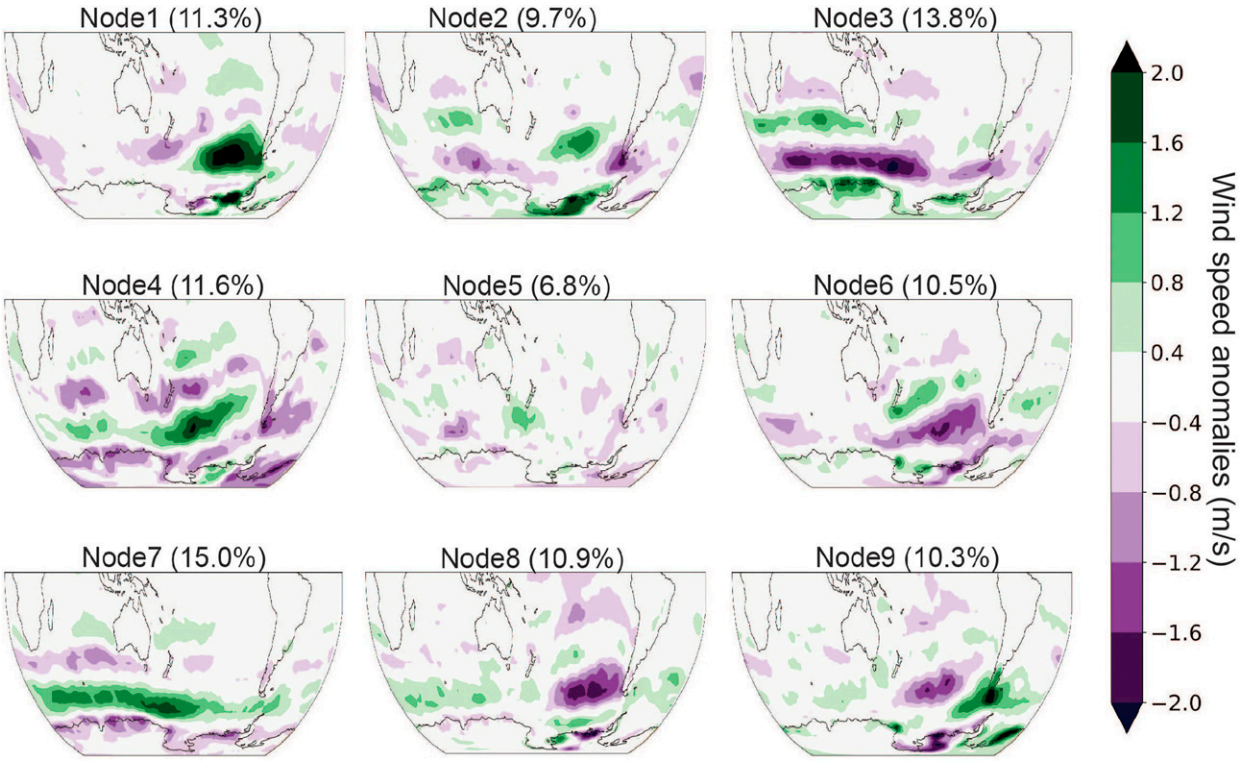

FIG. 7. Wind speed anomalies (m s^{-1}) corresponding to SOMs shown in Fig. 5. The purple colors represent negative wind speed anomalies, and the green colors show positive wind speed anomalies.

5. SAM as a driver of Tasman Sea marine heatwaves

a. Statistical analysis

From our SOM analysis, we found a strong connection between MHWs in the Tasman Sea and the positive SAM phase that presents as an atmospheric wave-3 pattern. It has been previously noted that there is a significant correlation between the negative phase of ENSO and the positive phase of SAM, especially during austral spring months (Fogt et al. 2011; Yu et al. 2015; Dätwyler et al. 2020). Campitelli et al. (2022) found that this connection could be entirely explained by the version of positive SAM that presents as an atmospheric wave-3 pattern, which they named the asymmetric SAM (A-SAM). A second version of positive SAM, presenting as the commonly known pattern of negative MSLP anomalies over Antarctica, with a zonally symmetric ring of positive anomalies at mid- to high latitudes, is called the symmetric positive SAM (S-SAM).

We followed the same method as Campitelli et al. (2022) to calculate the A-SAM as its own index. Starting with the leading EOF of monthly MSLP anomalies, we removed the zonally averaged pattern (S-SAM) and projected the daily MSLP anomalies back onto the remaining pattern to calculate a daily index to be used for the correlation analysis.

To understand the impact of A-SAM on ocean temperatures in the Tasman Sea, the daily SST anomaly data were first processed to remove any linear trends and the influence of ENSO. The imprint of Niño-3.4 onto SSTs in the Australian region was calculated using linear regression, and the resulting anomalies were removed from the original data to produce a new dataset of SST anomalies independent of Niño-3.4. For more specific details on the method applied, see Werner et al. (2012).

Figure 9 shows the correlation between this new SST anomaly dataset and the A-SAM index during the austral spring months (SON; Fig. 9a) and austral summer months (DJF; Fig. 9b). To account for the serial correlation inherent in geophysical data, we consider the autocorrelation ρ of SST anomalies at each grid cell to calculate the effective sample size $n_{\text{eff}} = n(1 - \rho)/(1 + \rho)$ (see Marshall et al. 2014). This effective sample size was used to calculate the t statistic and assess statistical significance using a two-tailed t test. Only statistically significant relationships are shaded ($p < 0.05$), with the correlations indicating a significant relationship between the positive A-SAM and positive SST anomalies in the Tasman Sea, after removal of the ENSO signal (i.e., ENSO independent).

b. Dynamic–thermodynamic interpretation

To understand the dynamic–thermodynamic connection between the A-SAM and Tasman Sea MHWs, we examined the significant anomalies of several atmospheric variables during strong and positive spring A-SAM days (where the A-SAM index is greater than 1.5 standard deviations from the mean). Figure 10 shows anomalies of the important components of the air–sea heat fluxes: 1) net latent heat flux and 2) net downward solar radiation at the sea surface (which is strongly influenced by the cloud cover), together with the 3) wind speed

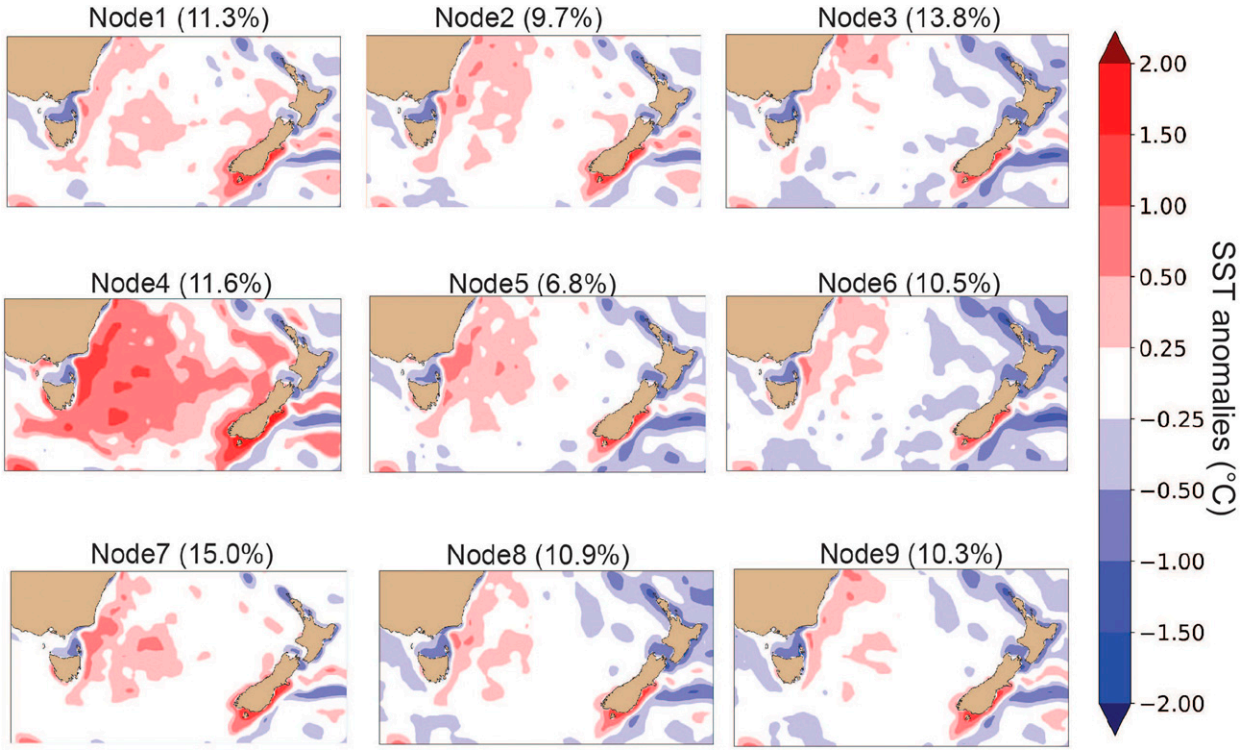

FIG. 8. SST anomalies (°C) in the TS corresponding to the SOMs shown in Fig. 5. Although most of the nodes show a slight positive SST anomaly associated with the EAC, node 4 clearly displays the spatial pattern of MHWs driven by air–sea interactions (see Fig. 5, right).

anomalies and 4) SST anomalies, with statistical significance at the 5% levels assessed using a Student's t test (Student 1908). Scale analysis demonstrates that the other components of the air–sea heat flux, sensible heat, and downward thermal radiation, play a much less significant role and hence are not shown.

From these results, we can better understand how the A-SAM contributes to positive SST anomalies in the region. Latent heat loss from the ocean surface is directly related to the evaporative heat exchange, which cools the sea surface and warms the atmosphere through condensation and cloud formation (Taylor et al. 2003). Figure 10a shows the latent heat flux anomalies, with statistically significant positive values evident particularly in the eastern region of the TS box, as well as around Tasmania. Latent heat loss tends to increase with increased wind speeds (Zhang and Mcphaden 1995; Araligidad and Maloney 2008), and it appears that negative wind speed anomalies during these positive A-SAM events (Figs. 7 and 10c) are a key component of the positive temperature anomalies.

Blocking high pressure systems are associated with reduced cloud cover and higher surface exposure to solar radiation and are considered the major driver of atmospheric heatwaves (Brunner et al. 2017). The wavenumber-3 pattern,

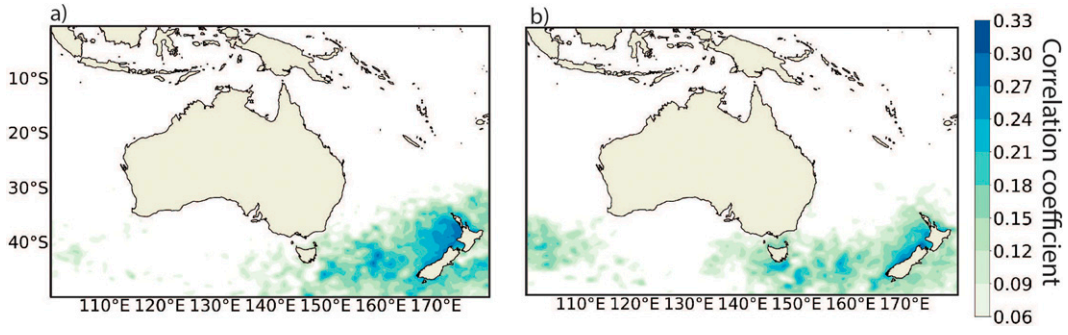

FIG. 9. Correlation between SST anomalies (with ENSO removed) and the positive A-SAM index during austral (a) spring (SON) and (b) summer (DJF). The maps only show statistically significant correlations at the >95% level ($p < 0.05$).

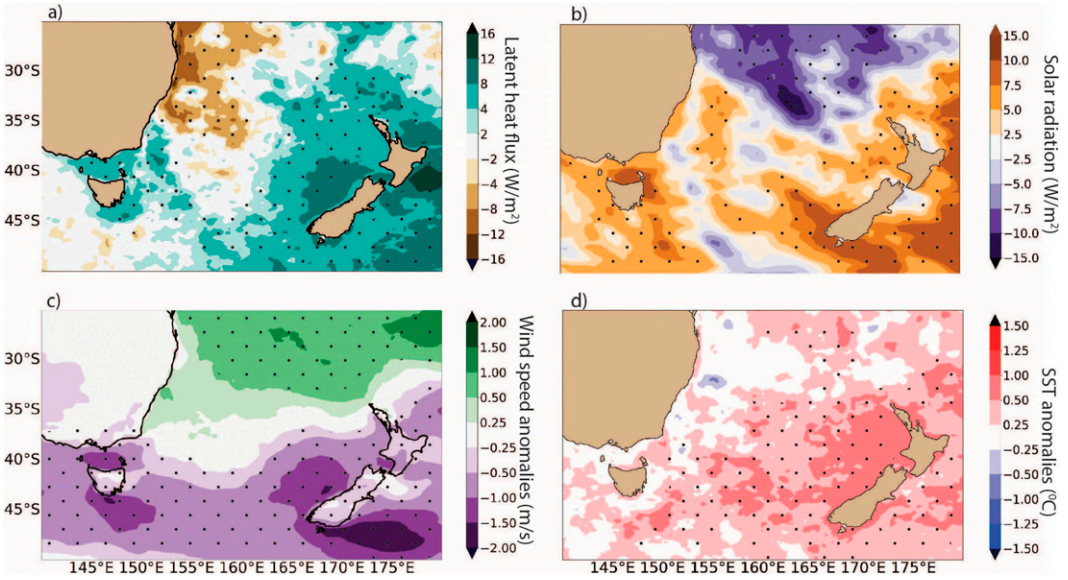

FIG. 10. Composite anomalies from BRAN2020 corresponding to positive A-SAM during spring (SON) between 1993 and 2021, showing the major components of the air–sea heat flux: (a) latent heat flux (W m^{-2}) and (b) solar radiation (W m^{-2}), (c) the anomalous wind speeds (shading) (m s^{-1}), and (d) SST anomalies (°C). Stippled areas show those regions of statistical significance with $p < 0.05$.

connected to the positive A-SAM phase, is a moving pattern of anomalous high and low pressure systems. The delayed response time of the ocean to the atmosphere results in the strongest SST anomalies developing in the Tasman Sea when these high pressure systems have passed the region and have their center just to the east of New Zealand (Fig. 6).

These dynamical links between the A-SAM and Tasman Sea MHWs are summarized in a schematic in Fig. 11. The top map shows the characteristic atmospheric blocking pattern present during A-SAM and the resulting positive SST anomalies in the Tasman Sea along with its association with La Niña conditions. The cylinder to the right in Fig. 11 represents the column of air above these high pressure cells, which allow both more solar radiation to reach the surface, due to reduced cloud cover, and anomalously high air temperatures to persist due to the warming from descending air. The box below shows the surface exposure to enhanced solar radiation, reduced wind speed anomalies, and associated reduced latent heat loss and vertical heat transport, and a shallower MLD trapping excess heat in the upper ocean (Fig. 11).

In summary, clearer skies associated with higher surface pressures permit more solar radiation to reach the surface. Acting with this enhanced solar radiation reaching the surface, decreased latent heat loss in a region of easterly wind anomalies (reduced westerly flow) on the equatorward flank of the high pressure system increases the total heat flux into (and gain by) the upper ocean. The resultant weaker surface winds and shallower mixed layer depth reduce the amount of heat being transported from the surface to depth, thus trapping heat in the upper layer of the ocean.

6. Summary and discussion

This paper has focused on understanding local atmospheric forcing of Tasman Sea MHWs in connection with large-scale atmospheric drivers. We first compared the properties of MHWs in the Tasman Sea driven primarily by ocean advection with those driven by atmospheric fluxes. Previous research found that approximately half of all events in the Tasman Sea are ocean advection driven, due to the extension of the warm poleward flowing EAC (Oliver et al. 2018b; Li et al. 2020, 2022b). Here, we have investigated the other half, driven by enhanced net downward heat fluxes. On average, these air–sea flux–driven events can be categorized as relatively short and sharp events (with an average of 16 days and a maximum intensity of 1.6°C), with a fast onset rate, shortening the potential preparation window for marine management responses, as outlined by Spillman et al. (2021).

Previous studies looking to understand the drivers of MHWs in a particular location have generally considered the processes occurring during the entirety of the events in question (e.g., Li et al. 2020; Schlegel et al. 2021). We have instead determined the drivers of each event by assessing the accumulation of heat during the onset phase, from the start to the peak date. This time window is important to identify the drivers of heat accumulation to an area and potentially beneficial for marine resource managers to be able to respond to such events (Spillman et al. 2021).

As the impacts of MHWs continue to worsen, particularly in "hotspot" regions, understanding their potential predictability has become increasingly important, in particular where accurate forecasts can be beneficial to mitigating impacts, such as within fisheries and aquaculture industries (Hobday

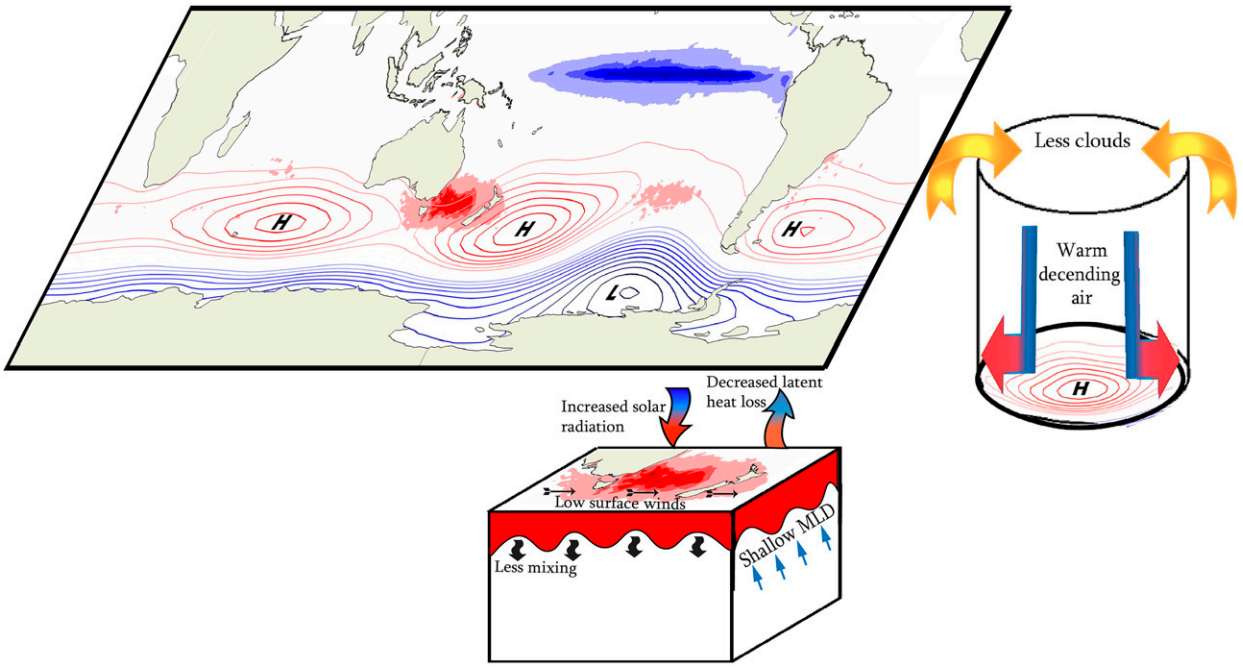

FIG. 11. Schematic summarizing the dynamic–thermodynamic explanation for the positive A-SAM influence on SST anomalies in the Tasman Sea. The map shows the positive SST anomalies (red) stretching across the TS and the contour lines showing the high and low pressure systems that form as a result of the positive A-SAM. The cooling pattern in the equatorial Pacific Ocean represents the La Niña conditions connected to both A-SAM and TS MHWs, particularly during austral spring. The cylinder depicts the atmospheric dynamics above these high pressure cells, with reduced cloud cover allowing a greater amount of solar radiation to reach the surface and more air descending and warming up as it reaches the surface. The box shows the processes occurring directly above and below the impacted area that contribute to heat becoming trapped in the upper layer of the ocean. Increased solar radiation and decreased latent heat loss increase the total heat through the surface, whereas weaker surface winds and a shallower MLD reduce the amount of heat being transported from the surface to depth.

et al. 2018b; Holbrook et al. 2020). The current management of marine resources will be better assisted with information about the likelihood of such extreme events on a time scale that allows for preparation and action, making accurate predictions at the subseasonal to seasonal time scale critical (Spillman and Hobday 2014).

The Tasman Sea is an important region for marine biodiversity, fisheries, and aquaculture industries in both Australia and New Zealand. First, our MHW calculations focused on the western Tasman Sea, closer to Australia, to allow for the assessment of MHWs within an area caused by enhanced advection in the EAC Extension and those that are atmospherically driven. We have shown that these two groups of MHWs have distinctly different properties that match those of their driver. In general, events that are driven by air–sea heat fluxes are short, sharp, and spatially extensive, with a rapid onset and decay. Conversely, MHWs driven by ocean advection tend to be longer in duration, less surface intensified, and smaller in spatial extent, with slower rates of onset and decay.

Our overall goal has focused on identifying the key atmospheric drivers of Tasman Sea MHWs, and as such, we have used surface ocean temperatures as the basis for our calculations. While subsurface data are necessary to perform a full heat budget analysis (e.g., Oliver et al. 2017) and understand the entire life cycle of an MHW (Elzahaby and Schaeffer 2019; Scannell et al. 2020; Elzahaby et al. 2021), data to the depth of the mixed layer are adequate to calculate statistics relevant to excess heat entering the ocean through air–sea interactions. Elzahaby et al. (2021) used subsurface data and a heat budget analysis to identify the drivers of MHWs in the Tasman Sea within a depth-dependent surface mixed layer. They found that advection-driven events are typically deeper, longer lasting below the surface, and more common during autumn and winter. Conversely, surface flux–driven events were more common during summer, coinciding with our result, when the likelihood of severe negative impacts on marine systems is enhanced. Although atmospherically driven events generally have a shallower vertical profile than their ocean advection–driven counterparts (Elzahaby et al. 2021), they have nevertheless been shown to cause substantial impacts to benthic communities. The atmospherically driven 2017/18 Tasman Sea MHW, for example, coincided with New Zealand's hottest summer on record (Perkins-Kirkpatrick et al. 2019; Salinger et al. 2019). However, its impacts extended well below the surface, including the decimation of bull kelp around the south island of New Zealand (Thomsen et al. 2019), loss of seaweeds (Thomsen and South 2019), and death of mussels (Salinger et al. 2020).

The profitability of marine industries is dependent on effective operational decision-making that is often based on probable environmental conditions. As many oceanic species are intrinsically linked to the seasonal thermal cycles of the ocean, catch and harvest strategies require reliable subseasonal to seasonal temperature predictions, underpinned by knowledge of how known modes of climate variability may alter these cycles. Insights into how various modes act together to impact regional climate is essential for understanding predictability at subseasonal to seasonal time scales. It has been established that there is a correlation between the negative phase of ENSO and the positive phase of SAM, particularly during austral spring (Fogt et al. 2011), with this relationship explained entirely by the A-SAM index, with a statistically significant correlation of −0.42 (Campitelli et al. 2022).

Chiswell (2021) recently found a connection between an atmospheric wavenumber-4 pattern and MHWs in the Southern Hemisphere. While he found that this atmospheric wavenumber-4 pattern was a key driver of MHWs in the Tasman Sea, he could not find any significant link to known modes of climate variability. In the present study, our SOMs analysis linked extensive MHWs in the Tasman Sea to the wavenumber-3 pattern, analogous with the A-SAM. Further analysis allowed us to find dynamical explanations for this relationship, as the location of the high pressure blocking systems formed during A-SAM provide ideal conditions to increase heat into the upper ocean, and prevent mixing to greater depths.

This connection is partially due to its weakening of the usually strong westerly winds in this region. Negative wind speed anomalies have been associated with the most extreme MHWs in the mid- to high latitudes (Sen Gupta et al. 2020), and we have found that all air–sea heat flux–driven MHWs in the Tasman Sea co-occur with lower-than-average surface winds. During the positive A-SAM phase, negative wind speed anomalies are present in the Tasman Sea, which contribute to increased SSTs due to the reduction of upper-ocean mixing, enabling heat to be retained near the surface rather than being transported to depth.

As drivers of MHWs are better understood (Holbrook et al. 2019), we become more aware of their potential predictability (Oliver et al. 2018b; Jacox et al. 2019; Holbrook et al. 2020). This, coupled with advances in ocean modeling capabilities, provides the opportunity to further incorporate seasonal forecasting, particularly around extreme events, into marine resource planning (Hobday et al. 2018b). Seasonal forecasting, based on dynamic coupled ocean–atmosphere models, has improved tremendously in recent times and can be useful to make environmental predictions several months into the future, informing management decisions (Hobday et al. 2016b). With global ocean warming being a primary reason for increases in MHWs (Oliver 2019), improved knowledge of MHW predictability on subseasonal to seasonal time scales, such as might be provided by connections between local forcing and large-scale atmospheric systems as identified in this study, will be of great benefit to marine industries attempting to mitigate the risks associated with such events.

Acknowledgments. We thank the three anonymous reviewers for their comments which helped us to significantly improve our paper. Author Gregory was supported by an ARC Centre of Excellence for Climate Extremes (CLEX) PhD scholarship, and additional top-up support from the joint CSIRO-UTAS Quantitative Marine Science program and Australian Bureau of Meteorology. Author Holbrook was supported by funding from the ARC Centre of Excellence for Climate Extremes (CE170100023) and the National Environmental Science Program Climate Systems Hub. Authors Marshall and Spillman acknowledge support from the Australian Bureau of Meteorology. Gregory acknowledges significant computational support from Australia's National Computational Infrastructure (NCI) and the CLEX Computational Modelling Support (CMS) team. We thank Danielle Udy for providing code and guidance for the SOM analysis. The authors declare that there are no known competing interests, whether personal, professional, or financial, that would influence the findings of this paper.

Data availability statement. All datasets used in this study are open source and available to be downloaded online. The OISSTv2 and NCEP–NCAR datasets were provided by the NOAA/OAR/ESRL PSL (https://psl.noaa.gov/). The BRAN202 dataset is publicly available online (https://dapds00.nci.org.au/thredds/catalog/gb6/BRAN/catalog.html). MHW event statistics were computed using the Python module (https://github.com/ecjoliver/marineHeatWaves), with the statistics calculated on each grid point using the modified xarray version (https://github.com/coecms/xmhw). EOF analysis was performed using the eof Python package (https://ajdawson.github.io/eofs/latest/) (Dawson 2016). For access to any of the code used, please contact the corresponding author.

REFERENCES

Australian Bureau of Agricultural and Resource Economics and Sciences, 2014: Australian fisheries and aquaculture statistics 2013. ABARES, accessed 10 February 2021, https://researchdata.edu.au/australian-fisheries-aquaculture-statistics-2013.

Allinson, N., H. Yin, L. Allinson, and J. Slack, 2012: *Advances in Self-Organising Maps*. Springer Science and Business Media, 289 pp.

Araligidad, N. M., and E. D. Maloney, 2008: Wind-driven latent heat flux and the intraseasonal oscillation. *Geophys. Res. Lett.*, **35**, L04815, https://doi.org/10.1029/2007GL032746.

Arias-Ortiz, A., and Coauthors, 2018: A marine heatwave drives massive losses from the world's largest seagrass carbon stocks. *Nat. Climate Change*, **8**, 338–344, https://doi.org/10.1038/s41558-018-0096-y.

Bamston, A. G., M. Chelliah, and S. B. Goldenberg, 1997: Documentation of a highly ENSO-related SST region in the equatorial Pacific: Research note. *Atmos. Ocean*, **35**, 367–383, https://doi.org/10.1080/07055900.1997.9649597.

Banzon, V., T. M. Smith, T. M. Chin, C. Liu, and W. Hankins, 2016: A long-term record of blended satellite and in situ sea-

surface temperature for climate monitoring, modeling and environmental studies. *Earth Syst. Sci. Data*, **8**, 165–176, https://doi.org/10.5194/essd-8-165-2016.

Benthuysen, J., M. Feng, and L. Zhong, 2014: Spatial patterns of warming off western Australia during the 2011 Ningaloo Niño: Quantifying impacts of remote and local forcing. *Cont. Shelf Res.*, **91**, 232–246, https://doi.org/10.1016/j.csr.2014.09.014.

Brunner, L., G. C. Hegerl, and A. K. Steiner, 2017: Connecting atmospheric blocking to European temperature extremes in spring. *J. Climate*, **30**, 585–594, https://doi.org/10.1175/JCLI-D-16-0518.1.

Campitelli, E., L. B. Díaz, and C. Vera, 2022: Assessment of zonally symmetric and asymmetric components of the Southern Annular Mode using a novel approach. *Climate Dyn.*, **58**, 161–178, https://doi.org/10.1007/s00382-021-05896-5.

Carton, J. A., S. A. Grodsky, and H. Liu, 2008: Variability of the oceanic mixed layer, 1960–2004. *J. Climate*, **21**, 1029–1047, https://doi.org/10.1175/2007JCLI1798.1.

Cassano, J. J., P. Uotila, and A. Lynch, 2006: Changes in synoptic weather patterns in the polar regions in the twentieth and twenty-first centuries, Part 1: Arctic. *Int. J. Climatol.*, **26**, 1027–1049, https://doi.org/10.1002/joc.1306.

Cetina-Heredia, P., M. Roughan, E. Van Sebille, and M. A. Coleman, 2014: Long-term trends in the East Australian Current separation latitude and eddy driven transport. *J. Geophys. Res. Oceans*, **119**, 4351–4366, https://doi.org/10.1002/2014JC010071.

Chamberlain, M. A., P. R. Oke, R. A. S. Fiedler, H. M. Beggs, G. B. Brassington, and P. Divakaran, 2021: Next generation of Bluelink ocean reanalysis with multiscale data assimilation: BRAN2020. *Earth Syst. Sci. Data*, **13**, 5663–5688, https://doi.org/10.5194/essd-13-5663-2021.

Chiswell, S. M., 2021: Atmospheric wavenumber-4 driven South Pacific marine heat waves and marine cool spells. *Nat. Commun.*, **12**, 4779, https://doi.org/10.1038/s41467-021-25160-y.

Cubasch, U., and Coauthors, 2001: Projections of future climate change. *Climate Change 2001: The Scientific Basis*, J. T. Houghton et al., Eds., Cambridge University Press, 526–582.

Cullen-Knox, C., A. Fleming, L. Lester, and E. Ogier, 2019: Publicised scrutiny and mediatised environmental conflict: The case of Tasmanian salmon aquaculture. *Mar. Policy*, **100**, 307–315, https://doi.org/10.1016/j.marpol.2018.11.040.

Dätwyler, C., M. Grosjean, N. J. Steiger, and R. Neukom, 2020: Teleconnections and relationship between the El Niño–Southern Oscillation (ENSO) and the Southern Annular Mode (SAM) in reconstructions and models over the past millennium. *Climate Past*, **16**, 743–756, https://doi.org/10.5194/cp-16-743-2020.

Dawson, A., 2016: EOFS: A library for EOF analysis of meteorological, oceanographic, and climate data. *J. Open Res. Software*, **4**, e14, https://doi.org/10.5334/jors.122.

Dufek, A. S., T. Ambrizzi, and R. P. Da Rocha, 2008: Are reanalysis data useful for calculating climate indices over South America? *Ann. N. Y. Acad. Sci.*, **1146**, 87–104, https://doi.org/10.1196/annals.1446.010.

Elzahaby, Y., and A. Schaeffer, 2019: Observational insight into the subsurface anomalies of marine heatwaves. *Front. Mar. Sci.*, **6**, 745, https://doi.org/10.3389/fmars.2019.00745.

——, ——, M. Roughan, and S. Delaux, 2021: Oceanic circulation drives the deepest and longest marine heatwaves in the East Australian Current system. *Geophys. Res. Lett.*, **48**, e2021GL094785, https://doi.org/10.1029/2021GL094785.

——, ——, ——, and ——, 2022: Why the mixed layer depth matters when diagnosing marine heatwave drivers using a heat budget approach. *Front. Climate*, **4**, 838017, https://doi.org/10.3389/fclim.2022.838017.

Fogt, R. L., D. H. Bromwich, and K. M. Hines, 2011: Understanding the SAM influence on the South Pacific ENSO teleconnection. *Climate Dyn.*, **36**, 1555–1576, https://doi.org/10.1007/s00382-010-0905-0.

Goddard, L., S. J. Mason, S. E. Zebiak, C. F. Ropelewski, R. Basher, and M. A. Cane, 2001: Current approaches to seasonal to interannual climate predictions. *Int. J. Climatol.*, **21**, 1111–1152, https://doi.org/10.1002/joc.636.

Gong, D., and S. Wang, 1999: Definition of Antarctic Oscillation index. *Geophys. Res. Lett.*, **26**, 459–462, https://doi.org/10.1029/1999GL900003.

Haigh, J. D., and H. K. Roscoe, 2006: Solar influences on polar modes of variability. *Meteor. Z.*, **15**, 371–378, http://doi.org/10.1127/0941-2948/2006/0123.

Hendon, H. H., D. W. J. Thompson, and M. C. Wheeler, 2007: Australian rainfall and surface temperature variations associated with the Southern Hemisphere Annular Mode. *J. Climate*, **20**, 2452–2467, https://doi.org/10.1175/JCLI4134.1.

Hobday, A. J., and G. T. Pecl, 2014: Identification of global marine hotspots: Sentinels for change and vanguards for adaptation action. *Rev. Fish Biol. Fish.*, **24**, 415–425, https://doi.org/10.1007/s11160-013-9326-6.

——, and Coauthors, 2016a: A hierarchical approach to defining marine heatwaves. *Prog. Oceanogr.*, **141**, 227–238, https://doi.org/10.1016/j.pocean.2015.12.014.

——, C. M. Spillman, J. Paige Eveson, and J. R. Hartog, 2016b: Seasonal forecasting for decision support in marine fisheries and aquaculture. *Fish. Oceanogr.*, **25**, 45–56, https://doi.org/10.1111/fog.12083.

——, and Coauthors, 2018a: Categorizing and naming marine heatwaves. *Oceanography*, **31**, 162–173, https://doi.org/10.5670/oceanog.2018.205.

——, C. M. Spillman, J. P. Eveson, J. R. Hartog, X. Zhang, and S. Brodie, 2018b: A framework for combining seasonal forecasts and climate projections to aid risk management for fisheries and aquaculture. *Front. Mar. Sci.*, **5**, 137, https://doi.org/10.3389/fmars.2018.00137.

Holbrook, N. J., and N. L. Bindoff, 1997: Interannual and decadal temperature variability in the southwest Pacific Ocean between 1955 and 1988. *J. Climate*, **10**, 1035–1049, https://doi.org/10.1175/1520-0442(1997)010<1035:IADTVI>2.0.CO;2.

——, and Coauthors, 2019: A global assessment of marine heatwaves and their drivers. *Nat. Commun.*, **10**, 2624, https://doi.org/10.1038/s41467-019-10206-z.

——, A. S. Gupta, E. C. J. Oliver, A. J. Hobday, J. A. Benthuysen, H. A. Scannell, D. A. Smale, and T. Wernberg, 2020: Keeping pace with marine heatwaves. *Nat. Rev. Earth Environ.*, **1**, 482–493, https://doi.org/10.1038/s43017-020-0068-4.

Huang, B., C. Liu, V. Banzon, E. Freeman, G. Graham, B. Hankins, T. Smith, and H.-M. Zhang, 2021a: Improvements of the Daily Optimum Interpolation Sea Surface Temperature (DOISST) Version 2.1. *J. Climate*, **34**, 2923–2939, https://doi.org/10.1175/JCLI-D-20-0166.1.

——, ——, E. Freeman, G. Graham, T. Smith, and H.-M. Zhang, 2021b: Assessment and intercomparison of NOAA Daily Optimum Interpolation Sea Surface Temperature (DOISST) Version 2.1. *J. Climate*, **34**, 7421–7441, https://doi.org/10.1175/JCLI-D-21-0001.1.

Jacox, M. G., D. Tommasi, M. A. Alexander, G. Hervieux, and C. A. Stock, 2019: Predicting the evolution of the 2014–2016 California Current System marine heatwave from an ensemble of coupled global climate forecasts. *Front. Mar. Sci.*, **6**, 497, https://doi.org/10.3389/fmars.2019.00497.

——, M. A. Alexander, S. J. Bograd, and J. D. Scott, 2020: Thermal displacement by marine heatwaves. *Nature*, **584**, 82–86, https://doi.org/10.1038/s41586-020-2534-z.

Kajtar, J. B., S. D. Bachman, N. J. Holbrook, and G. S. Pilo, 2022: Drivers, dynamics, and persistence of the 2017/2018 Tasman Sea marine heatwave. *J. Geophys. Res. Oceans*, **127**, e2022JC018931, https://doi.org/10.1029/2022JC018931.

Kalnay, E., and Coauthors, 1996: The NCEP/NCAR 40-Year Reanalysis Project. *Bull. Amer. Meteor. Soc.*, **77**, 437–471, https://doi.org/10.1175/1520-0477(1996)077<0437:TNYRP>2.0.CO;2.

Kanamitsu, M., W. Ebisuzaki, J. Woollen, S.-K. Yang, J. J. Hnilo, M. Fiorino, and G. L. Potter, 2002: NCEP–DOE AMIP-II Reanalysis (R-2). *Bull. Amer. Meteor. Soc.*, **83**, 1631–1643, https://doi.org/10.1175/BAMS-83-11-1631.

Karpechko, A. Y., N. P. Gillett, L. J. Gray, and M. Dall'Amico, 2010: Influence of ozone recovery and greenhouse gas increases on Southern Hemisphere circulation. *J. Geophys. Res.*, **115**, D22117, https://doi.org/10.1029/2010JD014423.

Kidston, J., J. A. Renwick, and J. Mcgregor, 2009: Hemispheric-scale seasonality of the Southern Annular Mode and impacts on the climate of New Zealand. *J. Climate*, **22**, 4759–4770, https://doi.org/10.1175/2009JCLI2640.1.

Kobayashi, S., and Coauthors, 2015: The JRA-55 Reanalysis: General specifications and basic characteristics. *J. Meteor. Soc. Japan*, **93**, 5–48, https://doi.org/10.2151/jmsj.2015-001.

Kohonen, T., 1990: The self-organizing map. *Proc. IEEE*, **78**, 1464–1480, https://doi.org/10.1109/5.58325.

L'Heureux, M. L., and D. W. J. Thompson, 2006: Observed relationships between the El Niño–Southern Oscillation and the extratropical zonal-mean circulation. *J. Climate*, **19**, 276–287, https://doi.org/10.1175/JCLI3617.1.

Li, J., M. Roughan, and C. Kerry, 2022a: Drivers of ocean warming in the western boundary currents of the Southern Hemisphere. *Nat. Climate Change*, **12**, 901–909, https://doi.org/10.1038/s41558-022-01473-8.

——, ——, and ——, 2022b: Variability and drivers of ocean temperature extremes in a warming western boundary current. *J. Climate*, **35**, 1097–1111, https://doi.org/10.1175/JCLI-D-21-0622.1.

Li, Z., N. J. Holbrook, X. Zhang, E. C. J. Oliver, and E. A. Cougnon, 2020: Remote forcing of Tasman Sea marine heatwaves. *J. Climate*, **33**, 5337–5354, https://doi.org/10.1175/JCLI-D-19-0641.1.

Limpasuvan, V., and D. L. Hartmann, 1999: Eddies and the annular modes of climate variability. *Geophys. Res. Lett.*, **26**, 3133–3136, https://doi.org/10.1029/1999GL010478.

Mariani, M., and M. S. Fletcher, 2016: The Southern Annular Mode determines interannual and centennial-scale fire activity in temperate southwest Tasmania, Australia. *Geophys. Res. Lett.*, **43**, 1702–1709, https://doi.org/10.1002/2016GL068082.

Marshall, A. G., D. Hudson, M. C. Wheeler, H. H. Hendon, and O. Alves, 2012: Simulation and prediction of the Southern Annular Mode and its influence on Australian intra-seasonal climate in POAMA. *Climate Dyn.*, **38**, 2483–2502, https://doi.org/10.1007/s00382-011-1140-z.

——, ——, ——, O. Alves, H. H. Hendon, M. J. Pook, and J. S. Risbey, 2014: Intra-seasonal drivers of extreme heat over Australia in observations and POAMA-2. *Climate Dyn.*, **43**, 1915–1937, https://doi.org/10.1007/s00382-013-2016-1.

Marshall, G. J., P. A. Stott, J. Turner, W. M. Connolley, J. C. King, and T. A. Lachlan-Cope, 2004: Causes of exceptional atmospheric circulation changes in the Southern Hemisphere. *Geophys. Res. Lett.*, **31**, L14205, https://doi.org/10.1029/2004GL019952.

Matthews, A. J., and M. P. Meredith, 2004: Variability of Antarctic circumpolar transport and the Southern Annular Mode associated with the Madden-Julian oscillation. *Geophys. Res. Lett.*, **31**, L24312, https://doi.org/10.1029/2004GL021666.

McPhaden, M. J., S. E. Zebiak, and M. H. Glantz, 2006: ENSO as an integrating concept in Earth science. *Science*, **314**, 1740–1745, https://doi.org/10.1126/science.1132588.

Oke, P. R., and Coauthors, 2013: Evaluation of a near-global eddy-resolving ocean model. *Geosci. Model Dev.*, **6**, 591–615, https://doi.org/10.5194/gmd-6-591-2013.

Oliver, E. C. J., 2019: Mean warming not variability drives marine heatwave trends. *Climate Dyn.*, **53**, 1653–1659, https://doi.org/10.1007/s00382-019-04707-2.

——, and N. J. Holbrook, 2018: Variability and long-term trends in the shelf circulation off eastern Tasmania. *J. Geophys. Res. Oceans*, **123**, 7366–7381, https://doi.org/10.1029/2018JC013994.

——, J. A. Benthuysen, N. L. Bindoff, A. J. Hobday, N. J. Holbrook, C. N. Mundy, and S. E. Perkins-Kirkpatrick, 2017: The unprecedented 2015/16 Tasman Sea marine heatwave. *Nat. Commun.*, **8**, 16101, https://doi.org/10.1038/ncomms16101.

——, and Coauthors, 2018a: Longer and more frequent marine heatwaves over the past century. *Nat. Commun.*, **9**, 1324, https://doi.org/10.1038/s41467-018-03732-9.

——, V. Lago, A. J. Hobday, N. J. Holbrook, S. D. Ling, and C. N. Mundy, 2018b: Marine heatwaves off eastern Tasmania: Trends, interannual variability, and predictability. *Prog. Oceanogr.*, **161**, 116–130, https://doi.org/10.1016/j.pocean.2018.02.007.

Perez, R., and Coauthors, 2013: Comparison of numerical weather prediction solar irradiance forecasts in the US, Canada and Europe. *Sol. Energy*, **94**, 305–326, https://doi.org/10.1016/j.solener.2013.05.005.

Perkins-Kirkpatrick, S. E., A. D. King, E. A. Cougnon, N. J. Holbrook, M. R. Grose, E. C. J. Oliver, S. C. Lewis, and F. Pourasghar, 2019: The role of natural variability and anthropogenic climate change in the 2017/18 Tasman Sea marine heatwave. *Bull. Amer. Meteor. Soc.*, **100**, S105–S110, https://doi.org/10.1175/BAMS-D-18-0116.1.

Philander, S. G. H., 1983: El Niño Southern Oscillation phenomena. *Nature*, **302**, 295–301, https://doi.org/10.1038/302295a0.

Raut, B. A., C. Jakob, and M. J. Reeder, 2014: Rainfall changes over southwestern Australia and their relationship to the Southern Annular Mode and ENSO. *J. Climate*, **27**, 5801–5814, https://doi.org/10.1175/JCLI-D-13-00773.1.

Reusch, D. B., R. B. Alley, and B. C. Hewitson, 2005: Relative performance of self-organizing maps and principal component analysis in pattern extraction from synthetic climatological data. *Polar Geogr.*, **29**, 188–212, https://doi.org/10.1080/789610199.

Reynolds, R. W., T. M. Smith, C. Liu, D. B. Chelton, K. S. Casey, and M. G. Schlax, 2007: Daily high-resolution-blended analyses for sea surface temperature. *J. Climate*, **20**, 5473–5496, https://doi.org/10.1175/2007JCLI1824.1.

Ridgway, K. R., 2007: Long-term trend and decadal variability of the southward penetration of the East Australian Current.

Geophys. Res. Lett., **34**, L13613, https://doi.org/10.1029/2007GL030393.

Risbey, J. S., M. J. Pook, P. C. Mcintosh, M. C. Wheeler, and H. H. Hendon, 2009: On the remote drivers of rainfall variability in Australia. *Mon. Wea. Rev.*, **137**, 3233–3253, https://doi.org/10.1175/2009MWR2861.1.

Rodrigues, R. R., A. S. Taschetto, A. Sen Gupta, and G. R. Foltz, 2019: Common cause for severe droughts in South America and marine heatwaves in the South Atlantic. *Nat. Geosci.*, **12**, 620–626, https://doi.org/10.1038/s41561-019-0393-8.

Rogers, J. C., and H. van Loon, 1982: Spatial variability of sea level pressure and 500 mb height anomalies over the Southern Hemisphere. *Mon. Wea. Rev.*, **110**, 1375–1392, https://doi.org/10.1175/1520-0493(1982)110<1375:SVOSLP>2.0.CO;2.

Salinger, M. J., and Coauthors, 2019: The unprecedented coupled ocean-atmosphere summer heatwave in the New Zealand region 2017/18: Drivers, mechanisms and impacts. *Environ. Res. Lett.*, **14**, 044023, https://doi.org/10.1088/1748-9326/ab012a.

——, and Coauthors, 2020: Unparalleled coupled ocean-atmosphere summer heatwaves in the New Zealand region: Drivers, mechanisms and impacts. *Climatic Change*, **162**, 485–506, https://doi.org/10.1007/s10584-020-02730-5.

Scannell, H. A., A. J. Pershing, M. A. Alexander, A. C. Thomas, and K. E. Mills, 2016: Frequency of marine heatwaves in the North Atlantic and North Pacific since 1950. *Geophys. Res. Lett.*, **43**, 2069–2076, https://doi.org/10.1002/2015GL067308.

——, G. C. Johnson, L. Thompson, J. M. Lyman, and S. C. Riser, 2020: Subsurface evolution and persistence of marine heatwaves in the northeast Pacific. *Geophys. Res. Lett.*, **47**, e2020GL090548, https://doi.org/10.1029/2020GL090548.

Schlegel, R. W., E. C. J. Oliver, and K. Chen, 2021: Drivers of marine heatwaves in the northwest Atlantic: The role of air–sea interaction during onset and decline. *Front. Mar. Sci.*, **8**, 627970, https://doi.org/10.3389/fmars.2021.627970.

Sen Gupta, A., and Coauthors, 2020: Drivers and impacts of the most extreme marine heatwave events. *Sci. Rep.*, **10**, 19359, https://doi.org/10.1038/s41598-020-75445-3.

Smale, D. A., and Coauthors, 2019: Marine heatwaves threaten global biodiversity and the provision of ecosystem services. *Nat. Climate Change*, **9**, 306–312, https://doi.org/10.1038/s41558-019-0412-1.

Smith, K. E., M. T. Burrows, A. J. Hobday, A. Sen Gupta, P. J. Moore, M. Thomsen, T. Wernberg, and D. A. Smale, 2021: Socioeconomic impacts of marine heatwaves: Global issues and opportunities. *Science*, **374**, eabj3593, https://doi.org/10.1126/science.abj3593.

Son, S.-W., N. F. Tandon, L. M. Polvani, and D. W. Waugh, 2009: Ozone hole and Southern Hemisphere climate change. *Geophys. Res. Lett.*, **36**, L15705, https://doi.org/10.1029/2009GL038671.

Spillman, C. M., and A. J. Hobday, 2014: Dynamical seasonal ocean forecasts to aid salmon farm management in a climate hotspot. *Climate Risk Manage.*, **1**, 25–38, https://doi.org/10.1016/j.crm.2013.12.001.

——, G. A. Smith, A. J. Hobday, and J. R. Hartog, 2021: Onset and decline rates of marine heatwaves: Global trends, seasonal forecasts and marine management. *Front. Climate*, **3**, 801217, https://doi.org/10.3389/fclim.2021.801217.

Student, 1908: The probable error of a mean. *Biometrika*, **6**, 1–25, https://doi.org/10.2307/2331554.

Taylor, C. M., R. J. Ellis, D. J. Parker, R. R. Burton, and C. D. Thorncroft, 2003: Linking boundary-layer variability with convection: A case-study from JET2000. *Quart. J. Roy. Meteor. Soc.*, **129**, 2233–2253, https://doi.org/10.1256/qj.02.134.

Thomsen, M. S., and P. M. South, 2019: Communities and attachment networks associated with primary, secondary and alternative foundation species; a case study of stressed and disturbed stands of southern bull kelp. *Diversity*, **11**, 56, https://doi.org/10.3390/d11040056.

——, L. Mondardini, T. Alestra, S. Gerrity, L. Tait, P. M. South, S. A. Lilley, and D. R. Schiel, 2019: Local extinction of bull kelp (*Durvillaea* spp.) due to a marine heatwave. *Front. Mar. Sci.*, **6**, 84, https://doi.org/10.3389/fmars.2019.00084.

Trenberth, K. E., 1979: Interannual variability of the 500 mb zonal mean flow in the Southern Hemisphere. *Mon. Wea. Rev.*, **107**, 1515–1524, https://doi.org/10.1175/1520-0493(1979)107<1515:IVOTMZ>2.0.CO;2.

Udy, D. G., T. R. Vance, A. S. Kiem, N. J. Holbrook, and M. A. J. Curran, 2021: Links between large-scale modes of climate variability and synoptic weather patterns in the southern Indian Ocean. *J. Climate*, **34**, 883–899, https://doi.org/10.1175/JCLI-D-20-0297.1.

Verdon-Kidd, D. C., and A. S. Kiem, 2009: On the relationship between large-scale climate modes and regional synoptic patterns that drive Victorian rainfall. *Hydrol. Earth Syst. Sci.*, **13**, 467–479, https://doi.org/10.5194/hess-13-467-2009.

Wang, Y., J. B. Kajtar, L. V. Alexander, G. S. Pilo, and N. J. Holbrook, 2022: Understanding the changing nature of marine cold-spells. *Geophys. Res. Lett.*, **49**, e2021GL097002, https://doi.org/10.1029/2021GL097002.

Weare, B. C., A. R. Navato, and R. E. Newell, 1976: Empirical orthogonal analysis of Pacific sea surface temperatures. *J. Phys. Oceanogr.*, **6**, 671–678, https://doi.org/10.1175/1520-0485(1976)006<0671:EOAOPS>2.0.CO;2.

Wehrens, R., and J. Kruisselbrink, 2018: Flexible self-organizing maps in Kohonen 3.0. *J. Stat. Software*, **87**, 1–18, https://doi.org/10.18637/jss.v087.i07.

Werner, A., A. M. Maharaj, and N. J. Holbrook, 2012: A new method for extracting the ENSO-independent Indian Ocean dipole: Application to Australian region tropical cyclone counts. *Climate Dyn.*, **38**, 2503–2511, https://doi.org/10.1007/s00382-011-1133-y.

White, C. J., and Coauthors, 2017: Potential applications of subseasonal-to-seasonal (S2S) predictions. *Meteor. Appl.*, **24**, 315–325, https://doi.org/10.1002/met.1654.

Xu, T., M. Newman, A. Capotondi, and E. Di Lorenzo, 2021: The continuum of northeast Pacific marine heatwaves and their relationship to the tropical Pacific. *Geophys. Res. Lett.*, **48**, 2020GL090661, https://doi.org/10.1029/2020GL090661.

Yu, J.-Y., H. Paek, E. S. Saltzman, and T. Lee, 2015: The early 1990s change in ENSO–PSA–SAM relationships and its impact on Southern Hemisphere climate. *J. Climate*, **28**, 9393–9408, https://doi.org/10.1175/JCLI-D-15-0335.1.

Zhang, G. J., and M. J. Mcphaden, 1995: The relationship between sea surface temperature and latent heat flux in the equatorial Pacific. *J. Climate*, **8**, 589–605, https://doi.org/10.1175/1520-0442(1995)008<0589:TRBSST>2.0.CO;2.

Zhang, T., S. Yang, X. Jiang, and P. Zhao, 2016: Seasonal–interannual variation and prediction of wet and dry season rainfall over the Maritime Continent: Roles of ENSO and monsoon circulation. *J. Climate*, **29**, 3675–3695, https://doi.org/10.1175/JCLI-D-15-0222.1.